Integrated High-Speed Wavelength Tracking on a Silicon Chip

Javier Elaskar, Simone Cammarata, Francesca Samà, Fabrizio Di Pasquale, and Claudio J. Oton

***Abstract*—A compact wavelength tracking device is integrated into a silicon photonic chip. The device involves an unbalanced Mach-Zehnder interferometer equipped with high-speed PN junction phase shifters operating in carrier-depletion mode. The system uses a modulation-demodulation scheme for reliable wavelength shift extraction on the measured optical signal. The noise standard deviation is $\sigma = 0.17$ pm, featuring a bandwidth of 150 kHz. Absolute wavelength measurements can be achieved within a 2 nm range. The device can also detect relative wavelength shifts in the 1520-1580 nm range. The proposed system finds applications in high-speed photonic sensing such as fast optical fiber Bragg grating sensor interrogation. Signal vibration detection at 42 kHz of a fiber Bragg grating sensor is also demonstrated.**

***Index Terms*—Fiber Bragg grating, high-speed sensing, Mach-Zehnder modulator, Mach-Zehnder interferometer, photonic integrated circuits, silicon photonics, wavelength measurement.**

I. INTRODUCTION

WAVEMETERS allow precise determination of the wavelength of narrow-band light signals emitted or reflected by optical devices. Generally, all the applications that require real-time monitoring of optical signals with varying spectral responses require wavemeters to track wavelength drifts. For this reason, they have become essential components in many fields, ranging from metrology, spectroscopy, sensing, and telecommunications, especially in the near infra-red (IR) spectral region [1], [2]. For instance, systems for light detection and ranging (LiDAR) are sometimes based on fast linear chirps in the emitted wavelength of tunable lasers [3]. In this case, accurate knowledge of the instantaneous wavelength is essential for the precise calculation of the target's range and velocity, as the wavelength modulation directly affects the measurement outcome [4]. Similarly, rapid laser tuning is harnessed in optical coherence tomography (OCT) to acquire depth-resolved images in biomedical sensing [5]. Monitoring the instantaneous wavelength ensures the accuracy and quality of these images, providing critical information for medical diagnosis and research. Moreover, wavelength-division multiplexed (WDM) optical networks require precise wavelength management to handle several data streams conveyed in the same transmission medium [6]. A rapid tracking of the instantaneous wavelength guarantees efficient and error-free data transmission.

Most of the available wavemeters are based on technologies that involve either interferometry, optical beating, or the properties of wavelength-dependent materials [7]. In some cases, the speckle pattern is used to get ultra-precise measurements [8]. Current commercial wavemeters rely mostly on bulk components with moving parts, which limits their durability, minimum size, and cost. A shift towards integrated devices could address all these drawbacks.

Silicon-integrated photonics offers high levels of integration, which allows the production of high-density photonic integrated circuits (PICs) at low cost. In recent years, many researchers have proposed different integrated detection systems to be used as wavemeters. In [9], an AWG is used to determine the wavelength of a laser using the center of mass technique, achieving 20 pm resolution over a 20 nm range; and [10] uses a similar technique with 2.5 pm resolution over 50 nm, but it requires an IR camera to read simultaneously over multiple ports. Another method is to use a linear filter, so that the received power at the photodiode is directly proportional to the wavelength, as in [11] where two multi-mode interferometers (MMIs) are used to create a linear filter to detect the wavelength with 15 pm resolution. However, they present considerable non-linearities.

Wavemeters can also measure Fiber Bragg Gratings (FBGs). FBGs are devices that reflect a narrow part of the spectrum, usually in the order of hundreds of pm. When used as sensors, the specific reflected wavelength shifts when the parameter they intend to measure varies. Some applications for FBGs include high-speed vibration detection for structural health monitoring and high-speed rotational parts. High-resolution and fast wavelength-measuring integrated devices thus become crucial even in optical fiber-based environmental sensing.

Recently, some works have been proposed to overcome the disadvantages of bulk devices using integrated photonics for FBG interrogation. For example, tunable micro-ring resonators equipped with on-chip heaters are used in [12] to retrieve

---

Received 22 August 2024; revised 11 November 2024; accepted 11 December 2024. Date of publication 16 December 2024; date of current version 2 April 2025. This work was supported in part by the PNRR-Investment 1.5 Ecosystems of Innovation, Project Tuscany Health Ecosystem (THE), Spoke 3 “Advanced technologies, methods, materials and health analytics”, under CUP: Grant I53C22000780001, and in part by the BRIEF “Biorobotics Research and Innovation Engineering Facilities” project under Grant IR0000036 funded under the National Recovery and Resilience Plan (NRRP), Mission 4 Component 2 Investment 3.1 of Italian Ministry of University and Research funded by the European Union – NextGenerationEU. *(Corresponding author: Javier Elaskar.)*

Javier Elaskar, Francesca Samà, Fabrizio Di Pasquale, and Claudio J. Oton are with the Scuola Superiore Sant'Anna, Institute of Mechanical Intelligence, 56124 Pisa, Italy (e-mail: j.elaskarplazas@santannapisa.it).

Simone Cammarata is with the Scuola Superiore Sant'Anna, Institute of Mechanical Intelligence, 56124 Pisa, Italy, and also with the Istituto Nazionale di Fisica Nucleare - Sezione di Pisa, 56127 Pisa, Italy.

Color versions of one or more figures in this article are available at https://doi.org/10.1109/JLT.2024.3517736.

Digital Object Identifier 10.1109/JLT.2024.3517736

the optical wavelength by tuning and matching the resonant wavelength of the ring with the maximum slope of the FBG [13], [14]. However, the detection range is limited by the free spectral range (FSR) of silicon-integrated ring resonators, which is usually no more than 20-30 nm [15]. Other wavelength interrogation techniques that accommodate a wider optical operational bandwidth use unbalanced Mach-Zehnder interferometers (MZIs) to detect the wavelength shift.

Nevertheless, using an unbalanced MZI without any modification has an inherent drawback related to its sinusoidal response in terms of wavelength. Indeed, depending on the working point of the MZI, the sensitivity of the output quantity to wavelength variations in the input signal might be poor, leading to the so-called *responsivity fading* when the MZI is away from the quadrature point. Different approaches and modifications to the standard unbalanced MZI have been proposed to overcome this effect. Passive interrogation methods involve using a 2x3 MMI as an output combiner for the interferometer to generate three 120-degree phased-shifted output signals [16] or using a 2x4 90-degree hybrid. In [17] multiple unbalanced MZIs are used with 90-degree hybrids to determine the absolute wavelength with 11 pm resolution over an 80 nm optical wavelength range centered at 1550 nm. However, passive interrogation techniques require multiple readout units, which ultimately hinders interrogation scalability as wavelength de-multiplexers, e.g., arrayed waveguide gratings (AWGs), would be required for each hybrid output. Instead, some active techniques only require the acquisition of one signal per sensor [18]. An example of an active technique is the well-known phase generated carrier (PGC) technique [19] where one arm of the MZI is modulated, and the phase is recovered through demodulation. An improved version of this demodulation technique called multi-tone mixing (MTM) is proposed in [20], where higher-order harmonics of the modulating frequency are harnessed for the phase retrieval of the output signal with reduced distortion.

In this work, we present a wavelength tracker with an on-chip unbalanced MZI, using the MTM technique for wavelength shift detection. The MZI is actively modulated by using PN junction-based phase shifters. In comparison with thermal phase shifters, free carrier-actuated devices have much greater bandwidth, over tens of GHz [21], and much better energy efficiency, at the expense of a larger footprint, larger driving voltages, and increased insertion losses [22].

In our previous work, [23] the active MTM technique was applied with a thermal phase modulator, which limited the maximum modulating signal frequency, thus limiting the system bandwidth below 1 kHz, and it was only used for FBG interrogation. In this work, the system bandwidth reaches 150 kHz, by using a PN phase modulator. In addition, we demonstrate wavelength tracking functionality besides FBG interrogation.

This paper is structured as follows. Section II describes the working principle of the proposed system for wavelength extraction and the associated phase modulation required by the active interrogation scheme. Section III presents the details of the implemented system along with the characterization of the MZI. In particular, the high-speed PN-junction phase shifter is characterized in three different driving configurations: series push-pull (SPP), push-pull (PP), and carrier injection (CI), to determine the optimal behavior in terms of linearity. In Section IV, the capabilities of the presented wavelength tracker are showcased in terms of resolution and tracking bandwidth using first a tunable laser and then a mechanically-actuated FBG. In both cases, the performances are compared against a commercial reference device. Finally, conclusions are drawn in Section V.

II. WORKING PRINCIPLE

An active MTM demodulation technique is used for phase extraction. A more detailed derivation of the method can be found in [20]. This technique introduces a sinusoidal phase modulation in the light passing through one of MZI's branches. This generates a current in the photodiode at the output of the MZI, which is described via the equation:

$$I = A + B\cos(\Delta\phi_{mod}) = A + B\cos(C\cos(\omega t) + \Delta\phi) \tag{1}$$

A and B are related to the interferometer mixing efficiency, C is the phase modulation depth, ω the modulation angular frequency, and $\Delta\phi$ the phase difference between the two branches of the MZI when it is not modulated. By expansion of (1) in terms of Bessel functions, the in-phase (I) and quadrature (Q) components can be respectively extracted from the even and odd harmonics of the modulating tone via the PGC:

$$I = A + B\{[f(\omega,t)]\cos(\Delta\phi) - [g(\omega,t)]\sin(\Delta\phi)\} \tag{2}$$

where

$$\begin{cases} f(\omega,t) = J_0(C) + 2\sum_{k=1}^{\infty}(-1)^k J_{2k}(C)\cos(2k\omega t) \\ g(\omega,t) = 2\sum_{k=0}^{\infty}(-1)^k J_{2k+1}(C)\cos((2k+1)\omega t) \end{cases}$$

Where J_i represents the bessel function of the first kind. When $C = 0.84\pi$ the first and second Bessel functions coincide and the phase can be recovered without distortion. The implementation of the MTM technique makes the system much more tolerant to deviations of the modulation depth C by taking into account higher harmonics of the modulating signal in the demodulation mixing phase. To this purpose, synthetic functions are digitally generated:

$$\begin{cases} f_1(t) = a_1\cos(\omega t) + a_3\cos(3\omega t) \\ f_2(t) = a_2\cos(2\omega t) \end{cases} \tag{3}$$

In the MTM technique up to the third harmonic, $a_1 = 1$, while a_2 and a_3 are obtained from the resolution of:

$$\begin{pmatrix} J_3(C) & J_2(C) \\ J_3'(C) & J_2'(C) \end{pmatrix}\begin{pmatrix} a_3 \\ a_2 \end{pmatrix} = \begin{pmatrix} J_1(C) \\ J_1'(C) \end{pmatrix} \tag{4}$$

For the nominal value of C, the solution is given by $a_2 = 2.5806$ and $a_3 = -3.0339$ [20], allowing the computation of:

$$\Delta\phi_{MTM} = \arctan\left(\frac{I \otimes f_1}{I \otimes f_2}\right) \tag{5}$$

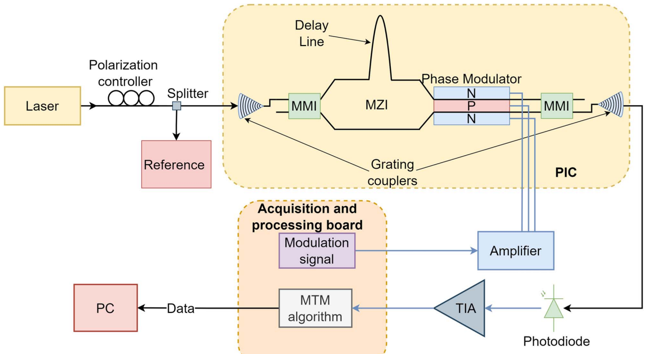

Fig. 1. Schematic diagram of the experimental setup. MMI: Multi-mode interferometer, MZI: Mach Zendher interferometer, PIC: Photonic integrated circuit, TIA: Trans-impedance amplifier.

with $\otimes$ representing the mixing operation, intended as a digital multiplication followed by a low-pass filter with a cut-off frequency lower than the modulating one.

The wavelength shift can now be calculated as:

$$\Delta\lambda = \frac{\Delta\phi_{MTM}}{2\pi}\Delta\lambda_{FSR} \tag{6}$$

Where $\Delta\lambda_{FSR}$ is the free-spectral range of the MZI in wavelength units. It is worth noting that absolute wavelength measurements can only be done inside an FSR-wide portion of the spectrum. However, relative wavelength shifts beyond one FSR can still be detected by unwrapping $\Delta\phi_{MTM}$.

III. SYSTEM DESIGN AND CHARACTERIZATION

A. Setup

The experiment setup is depicted in Fig. 1. Light is generated with a tunable laser (Santec TSL-570) operating from 1500 nm to 1630 nm with an output optical power of 7 dBm. This continuous-wave (CW) optical signal is then sent to a polarization controller to maximize the optical power coupled into the photonic integrated circuit (PIC) under test. Optical fiber-to-PIC coupling is indeed implemented with polarization-sensitive grating couplers.

Before entering the PIC, a 90/10 optical splitter divides the light to send 10% of the laser power to a reference. This reference component is the commercial interrogator model IBSEN I-MON 512 USB. It is configured with a sample rate of 2.5 kS/s and it is accessed through an optical attenuator to avoid its saturation. The IBSEN works primarily as an FBG interrogator, but it can also be used as a laser wavemeter. The remaining 90% of the CW light is sent to the silicon chip.

The PIC is designed in a silicon-on-insulator (SOI) technology characterized by 2 μm-thick buried oxide (BOX) and 220 nm-thick silicon device layer. The PIC is manufactured through a multi-project wafer (MPW) run at the Advanced Micro Foundry (AMF) facility. Electro-optic modulators are integrated into this technological platform thanks to the availability of silicon ion implantation process modules. A picture of the fabricated chip is shown in Fig. 2. Its overall dimension is 6x8 mm^2, while the footprint of the presented photonic circuit is 4x0.5 mm^2.

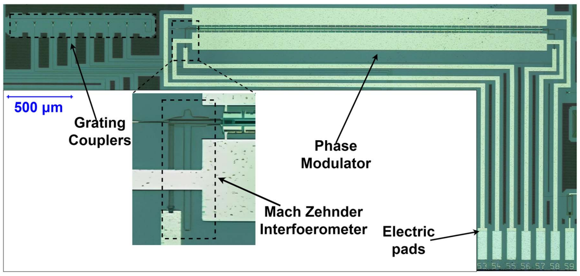

Fig. 2. Photo of the used circuit in the silicon chip taken by a microscope.

Light is coupled through grating couplers, and then a 2x2 multi-mode interferometer (MMI) is used to divide the light into the two branches of the MZI. The unbalanced MZI is designed with a length imbalance of approximately 290 μm between the two arms of the interferometer to obtain a free spectral range (FSR) of 2 nm. Both branches of the MZI are equipped with two 2.4 mm-long high-speed free-carrier-based phase shifters selected from the process design kit (PDK) provided by the foundry. As the free-carrier plasma dispersion effect is relatively weak in silicon, PN junctions are usually introduced in both arms to improve modulation performances [24], [25]. After the phase modulators, the two branches are recombined with a 2x2 MMI, effectively forming a conventional free-carrier-based Mach-Zehnder modulator (MZM) structure [22]. Finally, light is sent out of the PIC through another grating coupler.

After the MZM, the light coupled out of the PIC is sent to an InGaAs photodiode whose output signal is amplified with a trans-impedance amplifier (TIA) characterized by a gain of 3 kΩ gain and a bandwidth of around 18 MHz. This electrical signal is then sent to a data acquisition and processing system implemented with development board equipping a field-programmable gate array (FPGA) logic (Red Pitaya StemLab 125-14). This system acquires the signal from the TIA through an analog-to-digital converter (ADC) which runs at 125 MS/s sample rate.

The FPGA generates a sine-wave modulation signal at 1.3 MHz, which is sent to the phase modulator before being electrically amplified to meet the modulation amplitude requirements for the proposed device. The 1.3 MHz frequency was chosen as a good trade-off between being high enough to detect high-speed signals and low enough for a simple amplifier design. The FPGA hardware also performs the MTM demodulation. A digital low-pass filter with a corner frequency of 150 kHz is implemented to effectively reject the higher-order intermodulation products generated in the MTM processing stage [20]. The processed data are then sent to a PC.

All these processes are performed in real-time thanks to the FPGA-based hardware acceleration and the analyzed data is streamed to the PC at 1 MS/s. Further details regarding the FPGA implementation of the control and post-processing routines can be found in [26].

B. MZI and Phase Modulator Characterization

Fig. 3 shows the optical characterization of the MZI used for implementing the wavelength-shift extraction method described

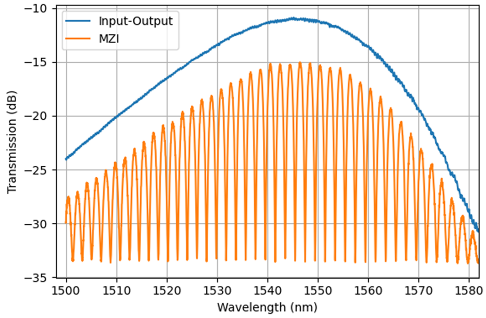

Fig. 3. Spectra of the input-output of the photonic chip through grating couplers and the MZI.

in Section II. The optical spectrum of the MZI is drawn in orange, while the blue line reports the spectrum of the light when it is coupled in and out of the PIC through grating couplers that are directly connected through a short waveguide loop of about 1.2 mm length.

The measured FSR of the MZI is close to 2 nm for wavelengths near 1550 nm, which is compliant with the design intentions. This means that absolute wavelength measurements are only possible within 2 nm because of the interference order uncertainty given by the periodic MZI spectrum. However, if only the wavelength shift is needed, unwrapping the extracted phase allows to measure beyond a single interference fringe, as it will be demonstrated in Section IV.

Three driving configurations of the MZM are tested to find the most suitable in terms of linearity and energy efficiency.

1) Series Push-Pull (SPP): In the SPP configuration, the cathode terminals of the modulator are connected to a variable voltage source and the common anode terminal is left unconnected, as shown in Fig. 4. To characterize the modulation efficiency of the MZM in this configuration, the voltage is changed from −12 V to 12 V in steps of 1 V. Given the symmetry of the electrical load, only one of the diodes is reversed-biased at the time and the allowed driving voltage can be symmetrically extended around 0 V. As expected, Fig. 4 shows that the phase shift normalized to the 0 V biasing condition is symmetric when changing the voltage bias polarity. In particular, the absolute phase variation that is achieved by changing bias is around 0.9π when going up to 12 V with voltage bias in both directions. Fig. 4 also reports a first-order polynomial fitting function for the phase shift versus voltage to inspect its linearity. The residual sum of squares (RSS) resulting from this fit is 0.0917, which is relatively high for the application of the MTM technique and suggests some non-linearities during the phase modulation. Also, the fringe contrast in the MZM decreases from 35 to 25 dB when the voltage is changed from 0 to 12 V or −12 V, indicating a certain degree of power imbalance between the two MZI arms which may result in modulation chirping [27].

2) Push-Pull (PP): In this case, the two PN junctions are both connected in reverse bias as shown in the schematic of fig 4. The common anode terminal is kept at a fixed voltage, with a low enough value so that the two diodes are never forward-biased. The voltage of the common anode was set to −6V (Vss in the figure), while the voltages of the cathodes (Vcc in the figure) were swept from −6 V to +6 V in steps of 1 V. In this case, the MZM's fringe contrast varies less than 5 dB between the different test voltages, which anticipates a more linear behavior. The relationship between voltage and phase shift is indeed shown in Fig. 4, together with a first-order polynomial fit. A better fit is obtained with respect to the previous case, as confirmed by the RSS value of 0.0036. This is due to the use of a dual-drive mode configuration so that the non-linearities of the diodes shown in the previous case are compensated with each other.

3) Carrier Injection (CI): The driving configuration schematic for testing the CI mode of the MZM's phase shifters is shown in Fig. 4. In this setup, only one PN junction is forward-biased and it is driven by a current source, which is swept from 0 mA to 6.5 mA in increments of 0.5 mA. As illustrated in Fig. 4, the MZM's fringe contrast difference between the 0 mA and 6.5 mA spectra is 8 dB, which is midway between the SPP and PP scenarios. In this configuration, the phase shift versus bias current can exceed π. However, at low-current driving ($<$ 0.5mA), the modulation efficiency is highly non-linear with respect to the bias current. Despite this non-linearity, when excluding this initial range, a first-order polynomial fit results in an RSS value of 0.0042, indicating a linearity performance similar to that seen in the PP driving configuration.

It is worth noting that in the CI case, the single-phase shifter power consumption ranges from 0.9 mW to 9.1 mW for driving currents in the 1 to 6.5 mA range. On the other hand, the reverse current passing through the diodes in SPP or PP driving configuration is always below 5 nA for all the biasing scenarios. This validates the ultra-low power consumption of the reverse-biased PN phase shifters which remains also in the μW scale.

According to this preliminary characterization, the modulator is operated in PP configuration with a differential driving circuit, as it provides the best linearity and power efficiency among the other alternatives.

IV. RESULTS AND DISCUSSION

The performance of the proposed wavelength tracker is first evaluated by inspecting its wavelength-tracking capabilities using a laser. The wavelength of the light emitted from a tunable laser source is linearly swept from 1520 nm to 1580 nm. The actual wavelength sweep range is above 60 nm, since the laser starts and ends the sweep above the set range due to a built-in configuration in the laser system. Our device can detect wavelength shifts beyond its 2 nm FSR thanks to an unwrapping algorithm applied to the phase retrieved from the MZI, which is only usable for relative wavelength shifts.

A first initial sweep was used to calibrate the device. With this calibration, the relation between the phase from our device and wavelength from the reference was fit with a second-order polynomial. This method for wavelength shift calculation is more precise than (6), as it takes into account the non-uniform $\Delta\lambda_{FSR}$ of the MZI, caused by the chromatic dispersion of the

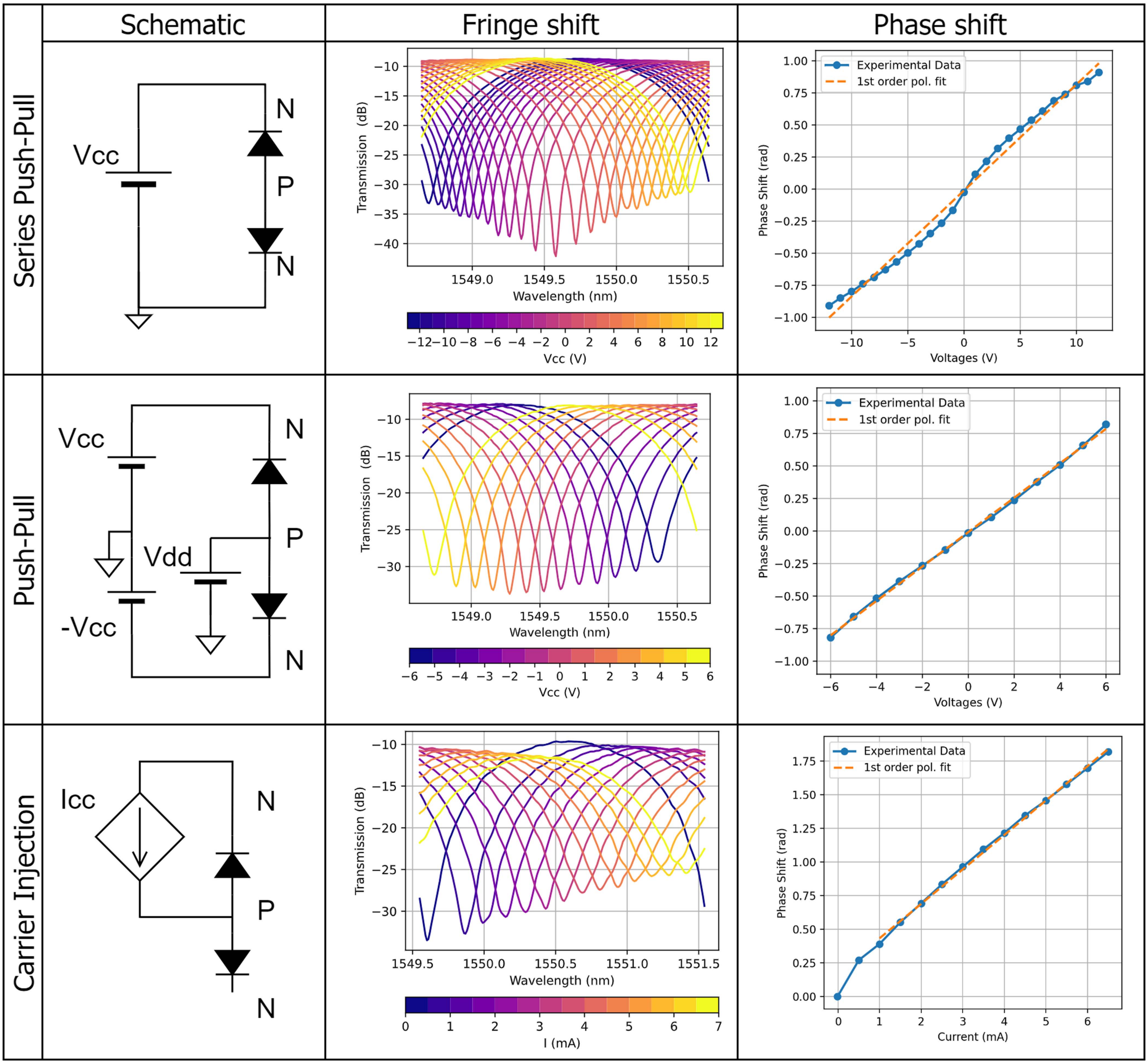

Fig. 4. Comparison of the series push-pull, push-pull, and carrier injection in 3 aspects: schematic, fringe shift, and phase shift.

waveguide. This polynomial was used in all the following experiments to calculate the wavelength from the retrieved phase. The reconstructed wavelength shift after the MTM processing on the device output signal is plotted in Fig. 5(a) together with the trace from the reference. It can be seen that there is a good fit between the reference device and ours. In Fig. 5(b), the difference between the two traces is shown. There is a maximum difference of 40 pm in the 60 nm sweep. It can be seen that there is a periodic component in this trace, that is likely to be generated from the small non-linearities of the PN modulator when used in Push-Pull, as shown in Fig. 4.

The wavelength shift detection is further assessed in dynamic conditions by applying a sinusoidal variation to the emitted laser wavelength. Fig. 6 shows the extracted wavelength shift of a 30 Hz tone which modulates the laser to induce a peak-to-peak wavelength variation of approximately 40 pm, with a difference between the reference and our device that oscillates around ± 1pm. According to the power spectral density (PSD) graph, there is a good match in the main frequency at 30 Hz and its even harmonics. The mismatch in the second harmonic can be attributed to the small non-linearity of the phase modulator.

To quantify the noise performance of the proposed wavelength tracker, the post-processed wavelength shift is tracked when the laser is kept at a fixed wavelength. Fig. 6 reports the time domain waveform associated and its PSD. The standard deviation of the temporal trace is 0.17 pm. In this case, the temporal trace of the reference interrogator is not shown since the two devices have different bandwidths. The reference interrogator is indeed

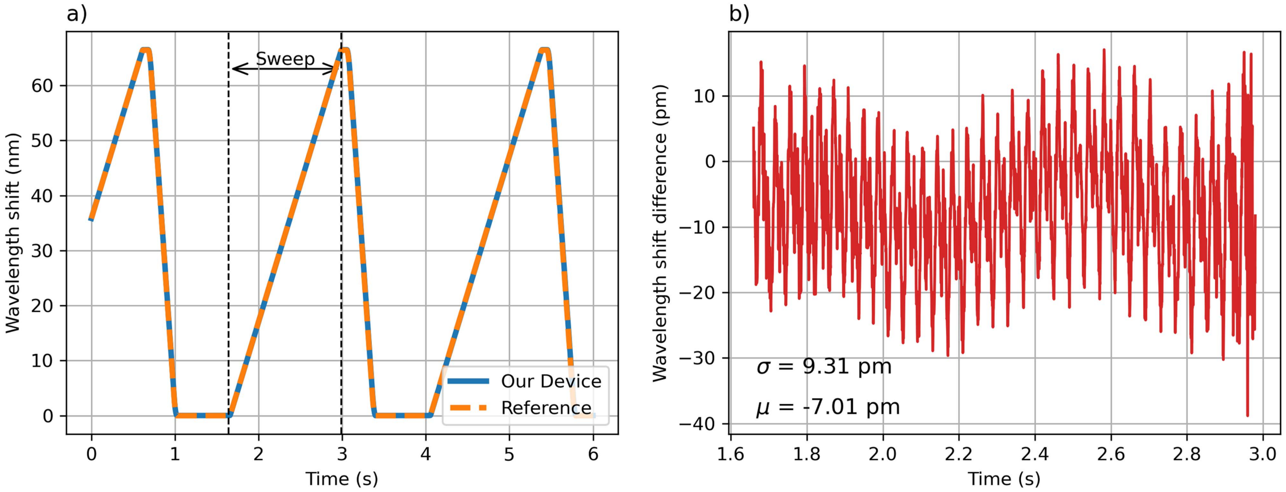

Fig. 5. (a) Comparison of laser wavelength shift measurement over 60 nm range between our device and the reference. (b) Difference between the devices. σ: Standard deviation, μ : Mean.

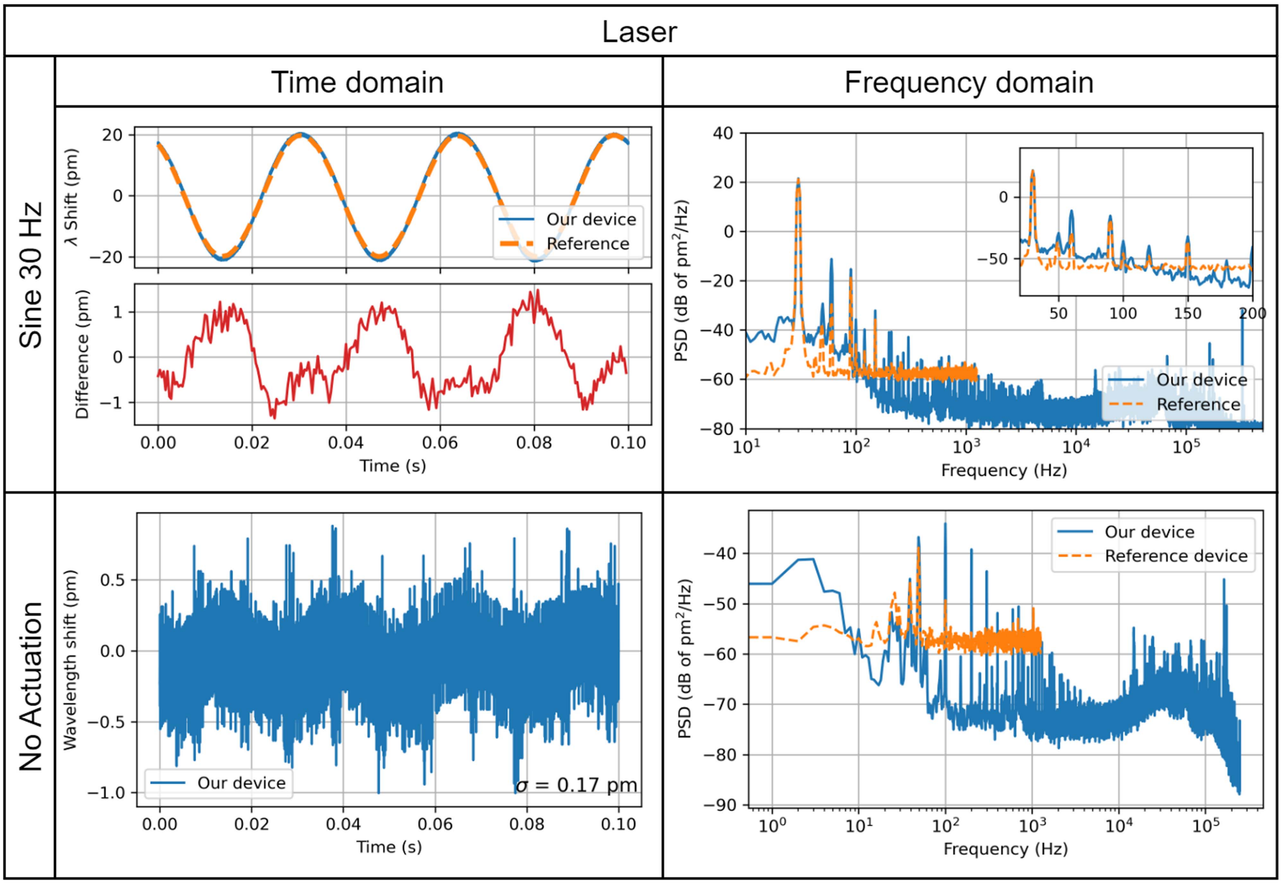

Fig. 6. Device used to measure the wavelength shift of the laser in the time and frequency domain. On the top, the laser is modulated with a 30Hz signal. On the bottom, the laser is at a static wavelength to measure the noise. λ : Wavelength.

characterized by a bandwidth of 1.5 kHz, which is largely lower than the 150 kHz bandwidth of our device, as shown in Fig. 6. Nevertheless, the noise levels can be compared through the PSD plots. For both devices, the 50 Hz interference from the grid line is the main source of interference, as well as its harmonics for our device. Although our device presents many spurious frequencies, the noise floor is about 10 dB lower than the reference interrogator.

To evaluate the usage of the proposed system to also work with another narrow-band light signal, the laser of Fig. 1 at the

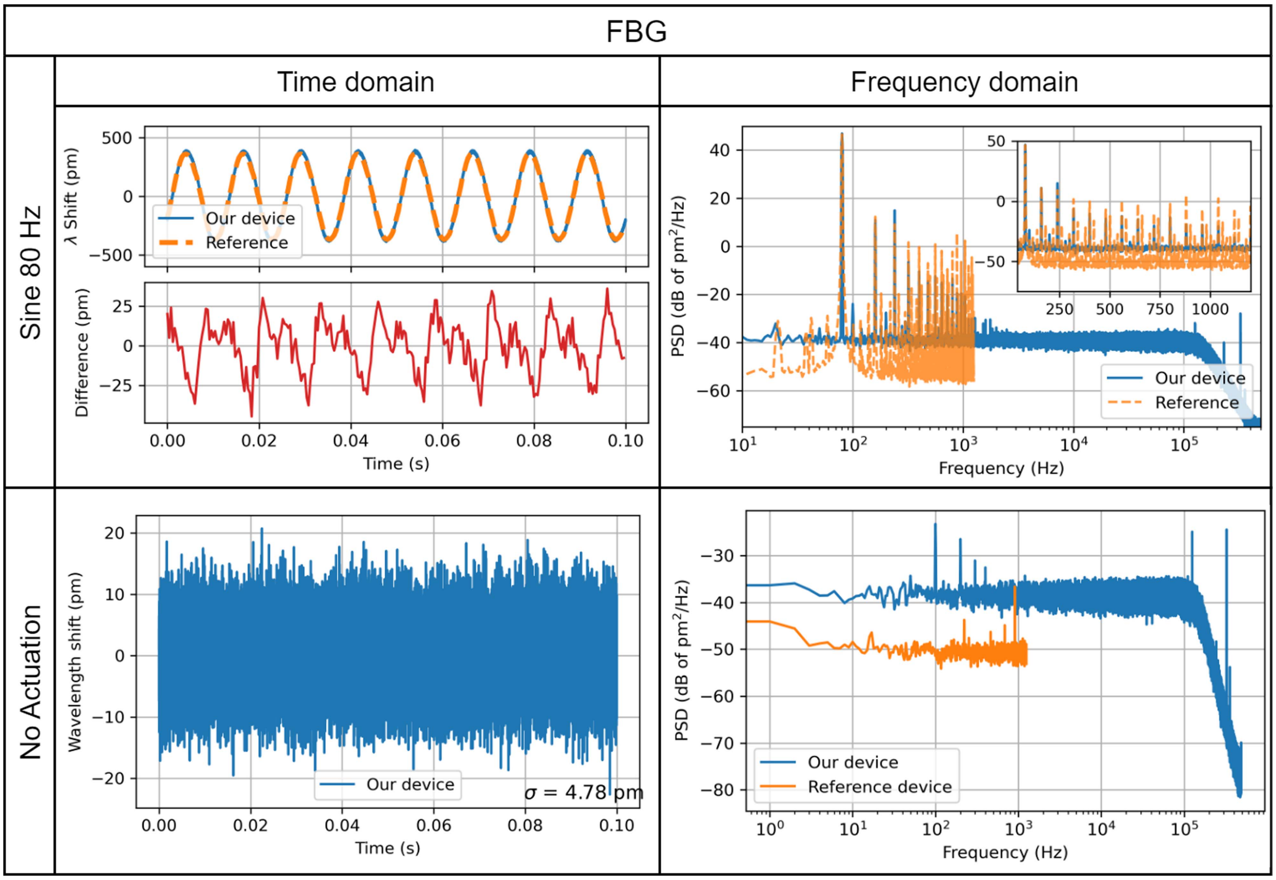

Fig. 7. Device used to measure the wavelength of an FBG at 1548 nm in the time and frequency domain. On the top, the FBG is modulated with an 80Hz signal. On the bottom, the FBG is at a static wavelength to measure the noise. λ : Wavelength.

input of the photonic chip was substituted with the light signal back-reflected from an FBG centered at 1548.5 nm with a full-width half-maximum (FWHM) of 0.28 nm, and a total reflected power of −14 dBm. The FBG is mounted on a piezoelectric actuator to induce a modulation of the reflected wavelength through strain. Fig. 7 shows the reconstructed wavelength shift corresponding to an 80 Hz sinusoidal modulation of the FBG reflected signal. The maximum difference between the traces is about 40 pm, and we consider it to be caused by the intrinsic error of our device, plus the error of the reference, caused mainly by aliased high-order harmonics of the signal. The frequency-domain PSD plots, show a few harmonics of the modulating signal that are detected in both interrogators. They are introduced by mechanical non-linearities coming from the piezoelectric actuation. Nevertheless, for the reference device, there are more spurious frequencies that are thought to be caused by aliased harmonics, which are not seen in our device thanks to the increased bandwidth. In this case, absolute wavelength measurements can be done as the FBG maximum shift is below 2 nm. It would just require a recalculation of the zero-degree term of the polynomial used for wavelength shift calculation.

Fig. 7 also shows a noise measurement of the proposed device used as an FBG interrogator, which is done by not exciting the piezoelectric. The calculated standard deviation of the extracted wavelength shift is 4.78 pm. The dynamic spectral resolution, defined as the noise standard deviation over the square root of the bandwidth is 12.3 fm/$\sqrt{Hz}$. Regarding the PSD noise of our device compared to the reference, both show flat noise floors with some spurious frequencies. In this case, unlike in the experiment with the swept laser, the reference interrogator has a lower noise floor, as shown in Fig. 7. This is due to the much weaker light power that enters the PIC in the FBG tracking experiment compared to the laser-driven scenario. According to our calculations, the white noise in the wavelength shift is inversely proportional to the input optical power. As there is approximately a 20 dB difference between the laser and FBG optical power, it corresponds to about a 40 dB difference in the noise floors of the laser and FBG in the PSD, as their scale is in pm^2 /Hz. This difference can be seen when comparing the noise floors of both sources. The power penalty caused by the grating couplers, shown in Fig 3, greatly affects the power received at the photodiode, and therefore, the noise of the device.

Finally, Fig. 8 shows the result when the piezoelectric is excited with a 42 kHz signal, which is its resonant frequency. The proposed wavelength tracker is able to detect this modulation frequency along with its first higher-order harmonic. From the corresponding PSD plot, it can be seen that the main modulation tone is detected with about 65 dB of SNR. The second harmonic,

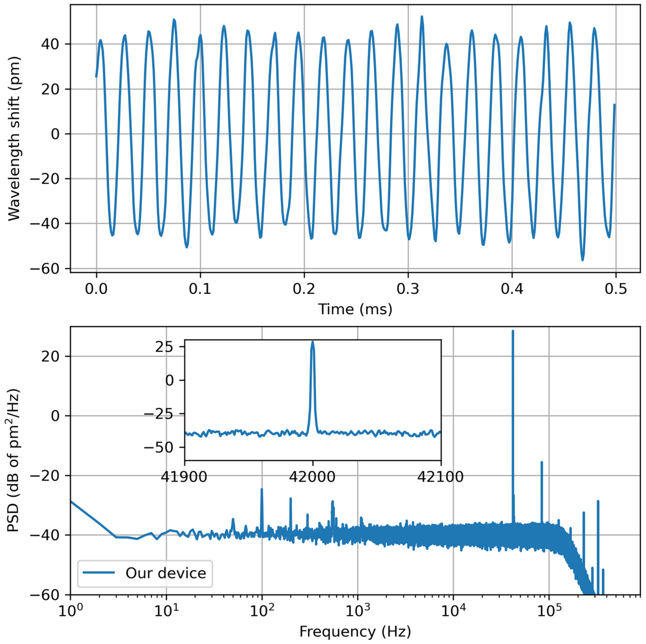

Fig. 8. FBG signal detection at 42 kHz.

detected at 84 kHz, can be likely attributed to the piezoelectric actuator, as in the previous experiment. In this case at 42 kHz, despite being its resonant frequency, the amplitude of the wavelength shift is about ten times lower than the 80 Hz case, as the piezoelectric is supposed to work up to 1 kHz. Due to the lower amplitude, the noise is more relevant in this case, and creates a noisier sinusoidal signal, as seen in the temporal trace.

V. CONCLUSION

We have demonstrated a prototype of an integrated on-chip wavelength tracking device with a 150 kHz bandwidth. Small shifts can be detected with high resolution thanks to its noise standard deviation of 0.17 pm. It can detect absolute wavelength shifts within a 2 nm range, and relative shifts in the 1520-1580 nm range. It can also be used as a high-speed FBG interrogator with a dynamic spectral resolution of 12.3fm/$\sqrt{Hz}$. The proposed device shows great potential in applications requiring a high degree of miniaturization or a low cost for high production volumes.

REFERENCES

[1] Y. Shimizu, L. C. Chen, D. W. Kim, X. Chen, X. Li, and H. Matsukuma, "An insight on optical metrology in manufacturing," *Meas. Sci. Technol.*, vol. 32, no. 4, 2020, Art. no. 042003.

[2] A. Z. Subramanian et al., "Silicon and silicon nitride photonic circuits for spectroscopic sensing on-a-chip," *Photon. Res.*, vol. 3, pp. B47–B59, 2015. [Online]. Available: https://opg.optica.org/prj/abstract.cfm?URI=prj-3-5-B47

[3] L. Tang, L. Li, J. Li, and M. Chen, "Hybrid integrated ultralow-linewidth and fast-chirped laser for FMCW LiDAR," *Opt. Exp.*, vol. 30, no. 17, pp. 30420–30429, Aug. 2022. [Online]. Available: https://opg.optica.org/oe/abstract.cfm?URI=oe-30-17-30420

[4] J. Yang et al., "High-ranging-precision FMCW LiDAR with adaptive predistortion of current injection to a semiconductor laser," *IEEE J. Lightw. Technol.*, vol. 42, no. 6, pp. 1870–1876, Mar. 2024.

[5] G. Yurtsever, N. Weiss, J. Kalkman, T. G. Van Leeuwen, and R. Baets, "Ultra-compact silicon photonic integrated interferometer for swept-source optical coherence tomography," *Opt. Lett.*, vol. 39, no. 17, pp. 5228–5231, Sep. 2014. [Online]. Available: https://opg.optica.org/ol/abstract.cfm?URI=ol-39-17-5228

[6] H. Debrégeas et al., "TWDM-PON burst mode lasers with reduced thermal frequency shift," *J. Lightw. Technol.*, vol. 36, no. 1, pp. 128–134, Jan. 2018.

[7] M. Dobosz and M. Kożuchowski, "Overview of the laser-wavelength measurement methods," *Opt. Lasers Eng.*, vol. 98, pp. 107–117, 2017.

[8] A. Dávila and J. Rayas, "Single-shot phase detection in a speckle wavemeter for the measurement of femtometric wavelength change," *Opt. Lasers Eng.*, vol. 125, 2020, Art. no. 105856.

[9] M. Muneeb et al., "Silicon-on-insulator shortwave infrared wavelength meter with integrated photodiodes for on-chip laser monitoring," *Opt. Exp.*, vol. 22, no. 22, pp. 27300–27308, 2014. [Online]. Available: https://opg.optica.org/viewmedia.cfm?uri=oe-22-22-27300&seq=0&html=truehttps://opg.optica.org/abstract.cfm?uri=oe-22-22-27300https://opg.optica.org/oe/abstract.cfm?uri=oe-22-22-27300

[10] A. Trita et al., "Simultaneous interrogation of multiple fiber Bragg grating sensors using an arrayed waveguide grating filter fabricated in SOI platform," *IEEE Photon. J.*, vol. 7, Dec. 2015, Art. no. 7802611.

[11] P. Wang et al., "Passive photonic integrated ratiometric wavelength monitor with resolution better than 15 PM," *Opt. Exp.*, vol. 25, 2017, Art. no. 2939.

[12] L. Tozzetti, F. Bontempi, A. Giacobbe, F. D. Pasquale, and S. Faralli, "Fast FBG interrogator on chip based on silicon on insulator ring resonator add/drop filters," *J. Lightw. Technol.*, vol. 40, 15, pp. 5328–5336, Aug. 2022.

[13] A. Shen et al., "Tunable microring based on-chip interrogator for wavelength-modulated optical sensors," *Opt. Commun.*, vol. 340, pp. 116–120, 2015.

[14] F. Yang, W. Zhang, S. Zhao, Q. Liu, J. Tao, and Z. He, "Miniature interrogator for multiplexed FBG strain sensors based on a thermally tunable microring resonator array," *Opt. Exp.*, vol. 27, no. 5, pp. 6037–6046, Mar. 2019. [Online]. Available: https://opg.optica.org/oe/abstract.cfm?URI=oe-27-5-6037

[15] W. Bogaerts et al., "Silicon microring resonators," *Laser Photon. Rev.*, vol. 6, no. 1, pp. 47–73, 2012, doi: 10.1002/lpor.201100017.

[16] M. Todd, M. Seaver, and F. Bucholtz, "Improved, operationally-passive interferometric demodulation method using 33 coupler," *Electron. Lett.*, vol. 38, 2002, pp. 784–786, Art. no. 784.

[17] B. Stern, K. Kim, H. Gariah, and D. Bitauld, "Athermal silicon photonic wavemeter for broadband and high-accuracy wavelength measurements," *Opt. Exp.*, vol. 29, 2021, Art. no. 29946.

[18] A. Ruocco and W. Bogaerts, "Fully integrated SOI wavelength meter based on phase shift technique," in *Proc. IEEE 12th Int. Conf. Group IV Photon.*, 2015, pp. 131–132.

[19] A. Dandridge, A. Tveten, and T. Giallorenzi, "Homodyne demodulation scheme for fiber optic sensors using phase generated carrier," *IEEE Trans. Microw. Theory Techn.*, vol. 30, no. 10, pp. 1635–1641, Oct. 1982.

[20] Y. Marin, P. Velha, and C. J. Oton, "Distortion-corrected phase demodulation using phase-generated carrier with multitone mixing," *Opt. Exp.*, vol. 28, pp. 36849, 2020.

[21] S. Cammarata, F. Palla, S. Saponara, F. D. Pasquale, P. Velha, and S. Faralli, "Compact silicon photonic Mach-Zehnder modulators for high-energy physics," *J. Instrum.*, vol. 19, no. 03, Mar. 2024, Art. no. C03009.

[22] S. Cammarata, P. Velha, F. Palla, F. Di Pasquale, S. Saponara, and S. Faralli, "30 Gb/s NRZ transmission with lumped-element silicon photonic mach-Zehnder modulator," in *Proc. 2022 IEEE Photon. Conf.*, 2022, pp. 1–2.

[23] J. Elaskar et al., "Ultracompact microinterferometer-based fiber Bragg grating interrogator on a silicon chip," *J. Lightw. Technol.*, vol. 41, no. 13, pp. 4397–4404, Jul. 2023.

[24] R. A. Soref and B. R. Bennett, "Electrooptical effects in silicon," *IEEE J. Quantum Electron.*, vol. 23, no. 1, pp. 123–129, Jan. 1987.

[25] S. Cammarata et al., "Design and performance evaluation of multi-Gb/s silicon photonics transmitters for high energy physics," *Energies*, vol. 13, no. 14, 2020, Art. no. 3569.

[26] J. Elaskar, M. Luda, L. Tozzetti, J. Codnia, and C. Oton, "FPGA-based high-speed optical fiber sensor based on multitone-mixing interferometry," *IEEE Trans. Instrum. Meas.*, vol. 71, 2022, Art. no. 7003011.

[27] D. Patel et al., "Design, analysis, and transmission system performance of a 41 GHz silicon photonic modulator," *Opt. Exp.*, vol. 23, no. 11, pp. 14263–14287, Jun. 2015. [Online]. Available: https://opg.optica.org/oe/abstract.cfm?URI=oe-23-11-14263

Javier Elaskar was born in Córdoba, Argentina, in 1994. He received the electronic engineering degree from the Universidad Nacional de Córdoba, Córdoba, Argentina, in 2018, and the dual master's degree in photonics and networking from Scuola Superiore Sant'Anna, Pisa, Italy, and Aston University, Birmingham, U.K., in 2021. He is currently working toward the Ph.D. degree in emerging digital technologies from Scuola Superiore Sant'Anna, with research topics related with optical fiber sensors and photonic integration.

Simone Cammarata received the B.Sc. and M.Sc. degrees (*cum laude*) in electronic engineering from University of Pisa, Pisa, Italy, in 2016 and 2019, respectively, and the Ph.D. degree in general information engineering from the Department of Information Engineering, University of Pisa, in 2024. Since 2017, he has been with the European Organization for Nuclear Research (CERN), Geneve, Switzerland, as an undergraduate student in the experimental physics - electronic systems for experiments group. Since 2022, he has been a Research Fellow with the Istituto Nazionale di Fisica Nucleare, Rome, Italy, and an Affiliate Researcher with the Istituto di Intelligenza Meccanica, Scuola Superiore Sant'Anna, Ghezzano, Italy, in the framework of a joint project focused on radiation-hard silicon photonics. His research interests mainly include integrated optics, high-speed electro-optic devices and interconnects, radiation effects in silicon photonic components, high-speed optical fiber sensing, and quantum silicon photonic circuits and systems.

Francesca Samà was born in 1999. She received the bachelor degree (*cum laude*) in mathematics from Università degli Studi della Campania "Luigi Vanvitelli", Napoli, Italy, in 2020. and the master's degree (*cum laude*) in mathematical engineering from Università degli studi di Napoli "Federico II", Naples, Italy. She is currently working toward the Ph.D. degree in emerging digital technologies with Scuola Superiore Sant'Anna, Pisa, Italy. In 2023, she was a Research Fellow with Scuola Superiore Sant'Anna Her research interests manily include photonic sensing and photonic integrated devices.

Fabrizio Di Pasquale received the degree in electronic engineering from the University of Bologna, Bologna, Italy, in 1989, and the Ph.D. degree in information technology from the University of Parma, Parma, Italy, in 1993. From 1993 to 1998, he was a Research Fellow with the Department of Electrical and Electronic Engineering, University College London, London, U.K., working on optical amplifiers, WDM optical communication systems, and liquid crystal displays. He was with Pirelli Cavi e Sistemi, Milan, Italy, and with Cisco Photonics, Vimercate, Italy, for two years and then moved to Scuola Superiore Sant'Anna, Pisa, Italy, where he is currently a Full Professor of telecommunications with the Institute of Mechanical Intelligence. He is the Co-Founder of Infibra Technologies S.r.l., a spin-off company of Scuola Superiore Sant'Anna, developing and marketing fiber optic sensor systems. He has authored or coauthored more than 250 scientific journals and conference papers and 25 patents. His research interests include optical fiber sensors, silicon photonics, optical amplifiers, WDM transmission systems and networks. He was the TPC Member of many international conferences and on the Board of Reviewers of international refereed journals.

Claudio J. Oton was born in Cartagena, Spain, in 1978. He received the degree in physics and the Ph.D. degree from the University of La Laguna, San Cristóbal de La Laguna, Spain, in 2000 and 2005, respectively. He spent four years as a Postdoctoral Researcher and Marie Curie Fellow with the Optoelectronics Research Centre, University of Southampton, Southampton, U.K. In 2009 he joined as a Senior Research Fellow with Nanophotonics Research Centre, Universidad Politecnica de Valencia, Valencia, Spain. In 2012, he joined as an Assistant Professor with Scuola Superiore Sant'Anna, Pisa, Italy, and from 2022, as an Associate Professor. He is with the Institute of Mechanical Intelligence, Monte Porzio Catone, Roma. His research interests mainly include photonic sensing with integrated photonics and optical fiber technologies. He has authored or coauthored more than 150 scientific papers and conferences, H-index 26, 3 patents, and has participated in many international research projects and contracts. He has been coordinator of projects funded by the Italian Space Agency, Italian Ministry of Economic Development, EU FP7 program, and has also coordinated many research contracts with industrial partners.

Open Access funding provided by 'Scuola Superiore "S.Anna" di Studi Universitari e di Perfezionamento' within the CRUI CARE Agreement